ADVANCED ENERGY MATERIALS
www.advenergymat.de

New Template Synthesis of Anomalously Large Capacity Hard Carbon for Na- and K-Ion Batteries

*Daisuke Igarashi, Yoko Tanaka, Kei Kubota, Ryoichi Tatara, Hayato Maejima, Tomooki Hosaka, and Shinichi Komaba**

Hard carbon (HC) is a promising negative-electrode material for Na-ion batteries. HC electrochemically stores Na^+ ions, resulting in a non-stoichiometric chemical composition depending on their nanoscale structure, including the carbon framework, and interstitial pores. Therefore, optimizing these structures for Na storage by altering the synthesis conditions can enhance the capacity of Na-ion batteries. In this study, HCs using MgO, ZnO, and $CaCO_3$ as nanopore templates are systematically investigated, and the ZnO template is found to be particularly effective. By optimizing the concentration of ZnO embedded in the carbon matrix, utilizing a blend of zinc gluconate, and zinc acetate as starting materials, the optimal ZnO-template HC demonstrates a reversible capacity of 464 mAh g^{-1} (corresponding to $NaC_{4.8}$) with high initial coulombic efficiency of 91.7% and low average potential of 0.18 V versus Na^+/Na. Thus, a Na-ion battery full cell consisting of $Na_{5/6}Ni_{1/3}Fe_{1/6}Mn_{1/6}Ti_{1/3}O_2$ and the optimized ZnO-template HC demonstrates a remarkable energy density of 312 Wh kg^{-1}, comparable to that of a Li-ion battery with $LiFePO_4$ and graphite. Moreover, the ZnO-template HC in a K half-cell also displays a significant capacity of 381 mAh g^{-1}, that is, $KC_{5.8}$ where the alkali content is higher than stage-1 graphite intercalation compounds, LiC_6 and KC_8.

1. Introduction

Na-ion batteries (NIBs) and K-ion batteries (KIBs) are emerging as next-generation batteries that eschew the use of minor and expensive elements such as Li, Co, and Cu. In recent years, these systems have attracted considerable attention as sustainable energy conversion technologies and future alternatives to Li-ion batteries (LIBs).[1,2] To develop practical NIBs, large-capacity electrode materials must be developed for achieving a performance comparable to that of LIBs. This is due to the inherent challenges of NIBs, such as relatively small capacity of alkali-containing positive electrode attributed to the three times heavier atomic weight of Na than Li and the lower voltage caused by the Na^+/Na potential being 0.2–0.3 V higher than that of Li^+/Li.[1]

Hard carbon (HC) is essentially non-graphitizable and emerges as one of the most promising negative electrode materials for NIBs.[3] Unlike LIBs, graphite cannot be used as a negative electrode in NIBs because of the thermodynamic instability of Na-graphite intercalation compounds (Na-GICs).[4] HC is a type of low-crystallinity carbon consisting of two different nanosized domain structures. One is a randomly oriented pseudo-graphitic domain composed of several stacked graphene sheets as a turbostratic structure with a variety of defects, and the other is internal micropores existing between pseudo-graphitic domains or graphene sheets as a nanosized interlayer space. The structure of HC varies and depends significantly on the raw material and heat treatment temperature. Generally, HCs prepared at higher temperatures have higher crystallinity in their pseudo-graphitic domains, larger pores, and fewer defects such as carbon defects and hetero-elements.[5–7] A unique feature of HC as a rechargeable battery material is its ability to store alkali metals such as Li and Na through the electrochemical formation of a non-stoichiometric composition[8,9] depending on the carbon structure. This is in contrast to graphite, where the maximum alkali metal storage capacity is determined by the stoichiometry of graphite intercalation compounds (GIC), such as LiC_6 and KC_8.[10,11] The non-stoichiometric process of alkali storage in HCs has the potential to exceed the capacity of graphite, even in Li and K cells. Since the 1990s, HC has been utilized as a negative electrode in the earliest LIBs,[12] and its application in KIBs continues to be a subject of ongoing research.[2]

D. Igarashi, Y. Tanaka, K. Kubota, R. Tatara, H. Maejima, T. Hosaka, S. Komaba
Department of Applied Chemistry
Tokyo University of Science
1-3 Kagurazaka, Shinjuku-ku, Tokyo 162-8601, Japan
E-mail: komaba@rs.tus.ac.jp
K. Kubota
Research Center for Energy and Environmental Materials (GREEN)
National Institute for Materials Science (NIMS)
1-1 Namiki, Tsukuba, Ibaraki 305-0044, Japan

The ORCID identification number(s) for the author(s) of this article can be found under https://doi.org/10.1002/aenm.202302647

DOI: 10.1002/aenm.202302647

Given that the structural characteristics of carbon materials are associated with their alkali-metal storage properties, new synthesis methods have been devised to control the structure of HCs and maximize their capacity as battery materials. For example, hetero-elements doping,[13,14] closing open pores on activated carbon, [15,16] bulk etching,[17] and template methods[15] have been reported after the simple strategy of changing the raw materials and heat treatment temperatures.[6] Although the detailed mechanism of Na insertion into HC is still under debate, recent studies, including various characterizations, and theoretical calculations of Na-inserted HC, have suggested the following sequence of three steps by sweeping from higher to lower potentials: 1) Na adsorption at various defect sites, 2) Na intercalation into the interlayers of pseudo-graphitic domains, and 3) the formation of quasi-metallic Na clusters within internal pores. In the final step, Na cluster formation in nanopores by applying a lower potential has been established by multiple groups through computational studies,[18–20] and experimental characterizations, including X-ray scattering methods,[3,21–24] solid state Na-NMR for chemical state analysis,[24–26] and other analyses, such as spectroscopy[27] and dilatometry.[7]

Based on these findings, the most intuitive approach for enhancing HC capacity is to design a pore structure optimized for Na storage. In line with this strategy, our group reported the synthesis of a HC with a reversible capacity of 478 mAh g^{-1}[15] using the MgO template method. In this process, MgO formed by the pyrolysis of Mg gluconate (Mg Glu) serves as a template for the formation of closed pores in the HC.[15] Although MgO is a well-known template material for controlling the structure of carbon,[28] other inorganic compounds such as zeolites,[29] silica,[30] ZnO,[31] and $CaCO_3$[32] have also been used to prepare mesoporous carbons.

In this study, we propose a new template carbon derived from gluconate salts of Zn and Ca, hereafter denoted as "Zn Glu" and "Ca Glu," respectively, to shed light on the potential of new template inorganics to synthesize HCs for NIBs and KIBs. The divalent nature of these three gluconate salts[33] serves as the starting material for synthesizing large-capacity HC materials, employing the same approach as that for the MgO-template carbon. Furthermore, we investigated the electrochemical properties of the template carbons as sodium and potassium insertion materials, considering that HCs with high Na storage capabilities often exhibit superior K storage properties, as per previous studies.

2. Results and Discussion

2.1. Synthesis and Characterization of Precursors

Figure 1a shows a schematic illustration of the HC synthesis process employed in this study, which is based on the concept of template synthesis methods from our recent study.[15] The chemical structures of the gluconate salts and starting materials are shown in Figure S1a (Supporting Information), and their powder morphologies observed by scanning electron microscopy (SEM) are shown in Figure S1b–d (Supporting Information). Gluconates are widely used as precursors for template carbons.[28] During the preheating process at 600 °C, the starting material was pyrolyzed and transformed into a composite of precursor carbon and inorganic particles, which served as the nanopore templates. In the subsequent acid leaching phase, excess inorganic particles on the carbon surface were eliminated, leaving open pores in their place. Through the final post-heating process in an inert atmosphere, the precursor carbon becomes HC, developing graphitic domains and closed nanopores.[34] Template oxides embedded in the carbon matrix of the precursor undergo reduction via a carbothermal reaction, forming elemental metals that are volatilized and removed at high temperatures.[35,36] The detailed sample preparation method is described in Supporting Information. Hereafter, the sample names of precursor carbons, washed precursor carbon via acid-leaching, and HCs as final products are referred to as "PRE-X," "wPRE-X," and "HC-X," respectively, where X represents the metal element in the starting material.

SEM images of both PRE-X and wPRE-X (X = Mg, Zn, or Ca) are shown in Figure S2 (Supporting Information). Notably, the morphology of PRE-X did not replicate that of the respective starting materials. Figure 1b shows a comparison of the X-ray diffraction (XRD) patterns of PRE-X and wPRE-X. The diffraction peaks of MgO, ZnO, CaO, and $CaCO_3$ are identified in the PRE-X pattern. In the wPRE-X pattern, however, the peak intensities of these inorganic materials noticeably diminished, and the broad peaks originating from low-crystalline carbon located at 2θ = 22 ° and 43 ° became relatively pronounced after acid leaching. This suggests that a significant proportion of the inorganic particles that served as templates was removed by acid leaching, which is consistent with the SEM-energy dispersive X-ray spectroscopy (EDS) analysis shown in Figure S3 (Supporting Information).

As reported in our earlier study on MgO-template carbon, the MgO in (w)PRE-Mg consists of small nanoparticles.[15] This was evident from the broad MgO peaks in the XRD patterns, and the MgO nanoparticles were distinctly visible in the dark-field transmission electron microscopy (TEM) image of PRE-Mg (Figure 1c).

By contrast, sharper ZnO-derived diffraction peaks are observed in the pattern of PRE-Zn, indicating the presence of highly crystalline ZnO with a larger particle size. However, the wPRE-Zn pattern shows broad ZnO peaks, suggesting that highly crystalline ZnO is primarily located on the carbon surface and can be removed by acid leaching. In fact, the SEM-EDS mapping in Figure S3 (Supporting Information) and the high-magnification SEM images of the PRE-Zn and wPRE-Zn samples in Figure S4 (Supporting Information) show white ZnO particles on PRE-Zn, whereas no such particles are visible in the SEM image of wPRE-Zn. Figure S5 (Supporting Information) presents a detailed analysis of the ZnO-derived diffraction peaks of PRE-Zn and wPRE-Zn. The 100, 002, and 101 diffraction peaks within 2θ = 30–40° in the patterns of PRE-Zn can be deconvoluted into sharp and broad components, whereas those of wPRE-Zn are fitted only with broad components. The ZnO crystallite size calculated through Scherrer's equation with the full width at half maximum (FWHM) of each 002 diffraction are 39.3 nm for the sharp component of PRE-Zn and 3.4 and 4.1 nm for the broad component of PRE-Zn and wPRE-Zn, respectively. The presence of ZnO nanoparticles in (w)PRE-Zn, as predicted from the XRD analysis, aligns with the dark-field TEM image of PRE-Zn shown in Figure 1d.

In the case of PRE-Ca, crystalline phases of both CaO and $CaCO_3$ were detected using XRD. Based on the literature, $CaCO_3$ is preferentially formed, and CaO is produced by the thermal

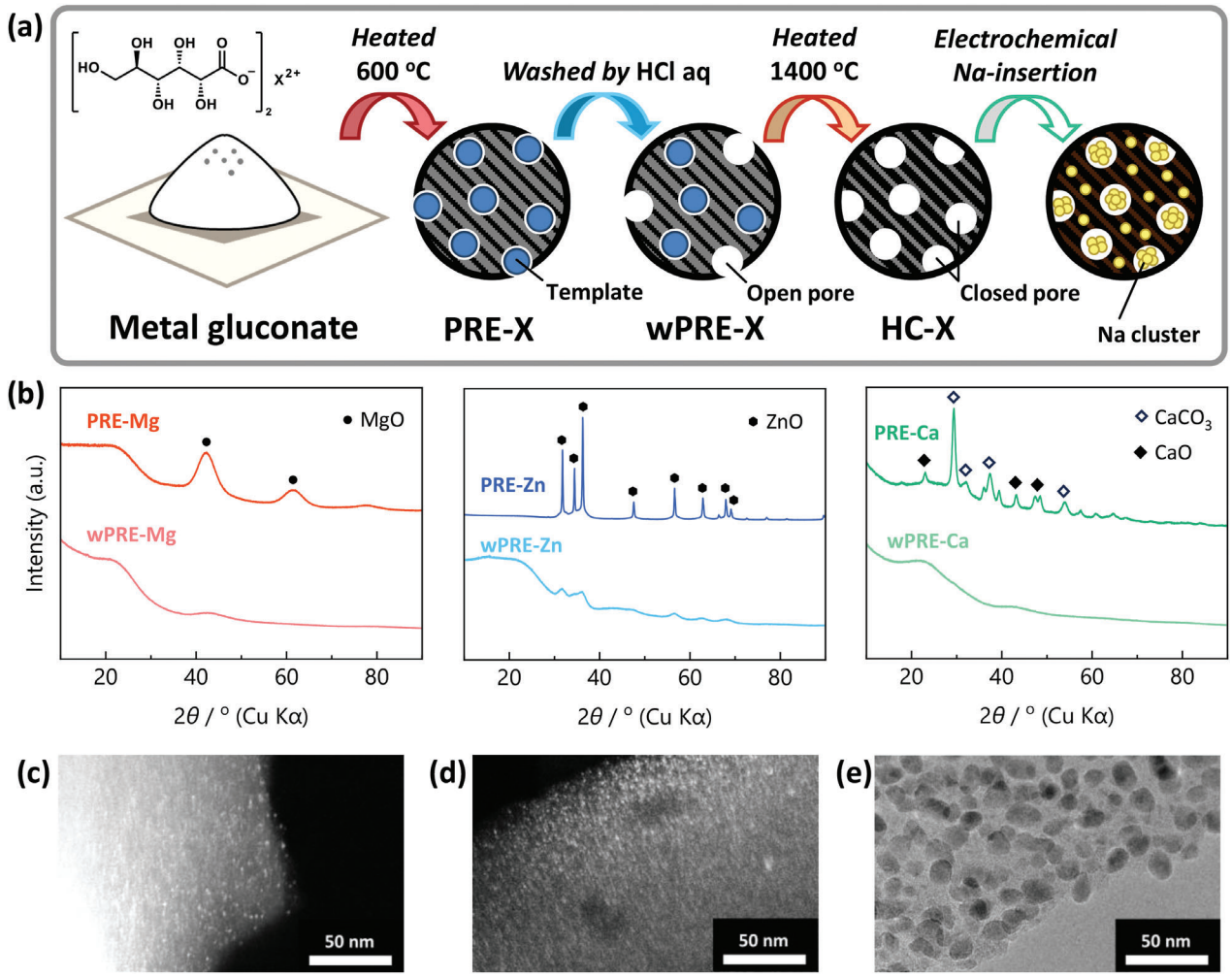

Figure 1. a) Illustration of template synthesis method. b) XRD patterns of PRE-X and wPRE-X, where X = Mg (left), Zn (middle), or Ca (right). Dark-field TEM images of c) PRE-Mg, and d) PRE-Zn, in which MgO and ZnO are indicated as bright spots. e) Bright-field TEM images of PRE-Ca.

decomposition of $CaCO_3$ under high-temperature conditions.[37] According to the TEM image in Figure 1e, the particle size of CaO or $CaCO_3$ in PRE-Ca is several tens of nanometers, which is considerably larger than that of MgO in PRE-Mg and ZnO in PRE-Zn and cannot serve as a "template" for the nanopores of HC.

As shown in the thermogravimetry-differential thermal analysis (TG-DTA) curves in Figure S6 (Supporting Information), the pyrolysis behaviors of Mg Glu, Zn Glu, and Ca Glu are different in terms of their exothermic and endothermic properties, as well as weight loss temperatures. Although the pyrolysis process of organic compounds is complex, making the decomposition process of each starting material difficult to discern in detail, these differences in pyrolysis behavior would affect the distribution and particle (crystallite) size of the inorganic particles, depending on the type of divalent metal involved.

2.2. Characterization of HCs

SEM images of the HCs synthesized from the three different gluconates are shown in **Figure 2**a. The morphology of each HC-X retained features of the corresponding wPRE-X (Figure S3, Supporting Information). The XRD patterns of HC-Mg, HC-Zn, and HC-Ca are shown in Figure 2b. All samples represented broad peaks typical for low-crystalline carbons at 2θ = 21–23° and 42–44°, which can be assigned to 002 and 100 diffractions, respectively, of pseudo-graphitic domains in HCs. The calculated average interlayer distances, d_{002}, are 0.3767, 0.3766, and 0.3564 nm for HC-Mg, HC-Zn, and HC-Ca, respectively. No peaks other than those of HC were observed in the XRD patterns, indicating that most of the templates were removed during the post-heat treatment process. The removal of the templates was also confirmed by STEM-EDS, as shown in Figure S7 (Supporting Information). Mg and Zn were barely detectable in HC-Mg and HC-Zn, while a small amount of Ca was detected in HC-Ca. Elemental mapping revealed the coexistence of dense Ca and O spots in the carbon matrix. Because the boiling point of metallic Ca is >1400 °C, it is presumed that it did not volatilize during the post-heat treatment and remained as CaO or $CaCO_3$.

The pore structures of the HCs were characterized using small-angle X-ray scattering (SAXS), as shown in Figure 2c. The

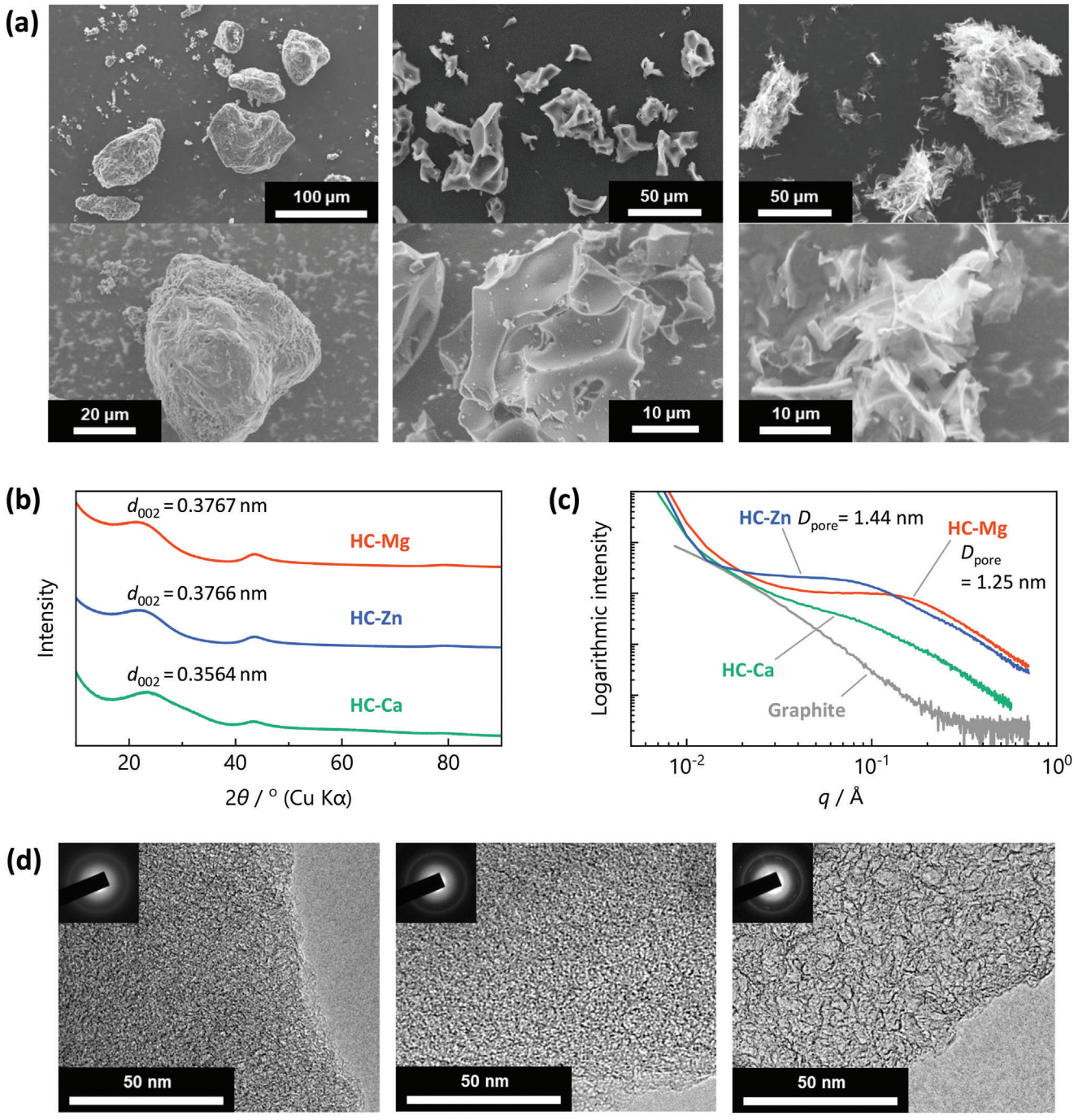

Figure 2. a) SEM images of HC-Mg (left), HC-Zn (middle), and HC-Ca (right). b) XRD patterns of HCs. c) SAXS patterns of HCs and graphite. d) HRTEM images of HC-Mg (left), HC-Zn (middle), and HC-Ca (right).

SAXS pattern of natural graphite is also displayed for comparison, as graphite does not contain pores. Notably, shoulder scattering peaks were clearly observed in the SAXS patterns of HC-Mg and HC-Zn. By pattern fitting and assumptions,[38] we calculated average pore sizes of 1.25 and 1.44 nm for the HC-Mg and HC-Zn samples, respectively. By contrast, the pattern for HC-Ca shows a shoulder peak with a very low intensity, which indicates that HC-Ca has a smaller or negligible number of closed pores than HC-Mg and HC-Zn. Based on our previous observations, the nanopore size of HCs obtained by simple carbonization of organic precursors at 1300–1500 °C is 1.1–1.2 nm,[6,39,40] therefore, HC-Mg and HC-Zn possess relatively larger sized nanopore structure. From these results, it can be concluded that the MgO and ZnO nanoparticles contained in PRE-Mg and PRE-Zn act as templates, enabling the formation of nanopores in HC-Mg and HC-Zn.

The pore structures of the HCs were further characterized by microstructural observations using high-resolution TEM (HRTEM), as shown in Figure 2d. The HRTEM images of PRE-Mg and PRE-Zn show dense microstructures on the scale of a few nanometers, whereas larger voids (5–10 nm in diameter) were observed in HC-Ca. Although the CaO or $CaCO_3$ particles formed in PRE-Ca may lead to the formation of these large voids, such large spaces are considered unsuitable for the electrochemical formation of Na clusters.[23,24]

N_2-sorption measurement of the HCs were conducted, and the observed isotherms of the HCs are displayed in Figure S8 (Supporting Information). A typical type-I isotherm was obtained for HC-Mg, whereas the isotherm for HC-Zn appeared to be type-II, but with a very small amount of N_2 adsorption. According to the IUPAC Technical Report, HC-Mg should have open micropores on its surface, while HC-Zn is a nonporous material or has only macropores.[41] The specific surface areas calculated based on Brunauer–Emmett–Teller (BET) theory (denoted as "S_{BET}") were 582 and 85 $m^2\ g^{-1}$ for HC-Mg and HC-Zn, respectively. The isotherm of HC-Ca shows a hysteresis loop from ambient pressure to the middle range of the relative pressure, which implies the presence of mesopores on the surface of HC-Ca. Although BET analysis is not entirely suitable for such materials, the tentative S_{BET} of HC-Ca, calculated from the adsorption curve, was 574 $m^2\ g^{-1}$. S_{BET} and the distribution of open pores calculated from gas sorption such as N_2 and CO_2 are often used to evaluate the "surface" structure of carbons, expecting that such insight into "surface" could be associated with passivation of electrode surface of solid electrolyte interphase (SEI) formation by covering with electrolytic decomposition products on the particles.[3] Considering that the solvent molecules and anions present in the electrolyte are larger than the N_2 or CO_2 molecules, the surface area determined by gas sorption does not necessarily represent the contact area between the liquid electrolyte and the electrode active material.[16,42] Therefore, we performed cyclic voltammetry (CV) on the HC electrodes to evaluate the contact areas in the potential range of 2.2–2.8 V versus Na^+/Na. This specific range was selected because of the absence of faradaic electrochemical reactions, while allowing for the formation of electric double layers at the electrode/electrolyte interface. The cyclic voltammograms obtained are shown in Figure S9 (Supporting Information). All the voltammograms show rectangular curves, which are typical characteristics of capacitors. The calculated average electric-double layer capacities in this potential range are 0.15 mAh g^{-1} for HC-Mg, 0.12 mAh g^{-1} for HC-Zn, and 0.97 mAh g^{-1} for HC-Ca (corresponding to 0.90, 0.72, and 5.8 F g^{-1}, respectively). These double-layer capacitance values are assumed to be linearly proportional to the contact area between the HC particles and the electrolyte solution. Therefore, we believe that the irreversible capacity of SEI formation on the HC electrodes in the Na cell is related to the capacitance, as described below.

2.3. Electrochemical Performance of HCs as NIB Negative Electrode

Charge–discharge tests (corresponding to the insertion and extraction of Na, respectively, at the HC electrode) were performed to evaluate the performance of the HC electrodes for NIBs. **Figure 3**a shows the initial charge–discharge curves of the HC electrodes in the Na half-cells. The HC composite electrodes show high reversible capacity of > 200 mAh g^{-1} with a voltage variation curve totally resembling those of other HC reported previously.[3] Thus, the redox activity of the template-synthesized HC electrodes is attributed to reversible sodium insertion.

Among the three samples, HC-Zn exhibited a superior battery performance, demonstrating an initial reversible capacity of 418 mAh g^{-1} and initial efficiency of 90%. HC-Mg also exhibits a high initial capacity and efficiency of 383 mAh g^{-1} and 85%, respectively; however, HC-Ca delivers a lower capacity of 258 mAh g^{-1} and an efficiency of 56% in the first cycle. The difference in reversible capacity can be explained by the characteristics of the closed pores evaluated by SAXS, that is, HC-Zn and HC-Mg show superior sodium storage performance compared to HC-Ca owing to their carbon structures with larger-sized closed pores and a higher proportion of closed pores. This is the first study to demonstrate that Zn-Glu-derived carbonaceous materials have remarkable properties as negative electrodes for rechargeable NIBs. This is notable because these materials have been previously studied in the context of other energy materials such as electrodes for double-layer capacitors,[43] and oxygen-reduction reaction catalysts.[44]

The capacities corresponding to the higher-potential slope region (>0.15 V) were 80, 89, and 81 mAh g^{-1}, and those of the lower-potential plateau region (<0.15 V) were 303, 329, and 177 mAh g^{-1} for HC-Mg, HC-Zn, and HC-Ca, respectively. The capacities and potential variations of the slope region were almost similar for each sample, ≈80 mAh g^{-1}, whereas the capacities of the plateau region differed among the three samples. This result aligns well with the material design; the pore structure design enhanced the formation of Na clusters and extended the plateau capacity at lower potentials. Other studies have also suggested that the nanopore structure of HC has a significant effect on the sodiation capacity in the plateau region.[7,23,45] The variation in the initial Coulombic efficiency of the HCs, related to irreversible electrolyte decomposition and SEI formation at the initial cycle, aligns more closely with the capacitances obtained from the CV discussed above rather than with the BET surface areas calculated from N_2 sorption, as shown previously. The smooth particle surface of Zn-HC observed by SEM (Figure 2a) likely contributed to reducing the contact area with the electrolyte, leading to a lower irreversible capacity and higher initial efficiency.

Figure 3b shows the cycle performance and corresponding coulombic efficiency of HC-Zn. Except for the first cycle, where electrolyte decomposition and SEI formation occurred in the early stages of sodiation, stable reversible cycling, and high efficiencies > 99% were obtained second cycle onward. These results demonstrate that the large reversible capacity does not include any plating/stripping of Na metal, which typically results in very low Coulombic efficiency in common electrolytes[46] but originates from reversible Na insertion into HC.

To confirm that the large capacity of HC-Zn originated from Na cluster formation in the nanopores, characterizations of sodiated HC electrodes were performed. Figure 3c shows the ex situ SAXS patterns of the pristine, fully sodiated, and fully desodiated HC electrodes. The intensity of the shoulder peak observed in the pristine sample decreased with sodiation and then increased again with desodiation, reverting to an intensity that

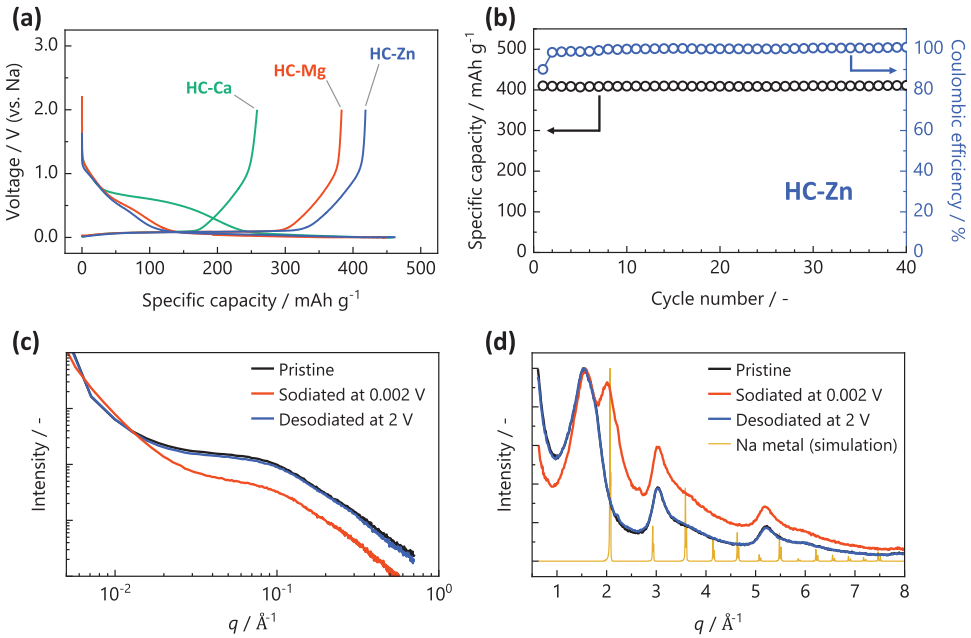

Figure 3. a) Initial charge–discharge curves of HCs. b) Cycle performance of HC-Zn. c) ex situ SAXS patterns of HC-Zn at different sodiation states. d) ex situ WAXS patterns of HC-Zn at different sodiation states.

closely aligned with the pristine state. The decreased peak intensity observed in the sodiated sample can be attributed to the reduced electron density contrast between the carbon matrix and pores, resulting from the insertion of Na atoms filling the nanopores.[3,21,22] The filling of the Na cluster is more clearly demonstrated in the ex situ wide-angle X-ray scattering (WAXS) patterns shown in Figure 3d, alongside the simulated scattering pattern of the Na metal crystal. The broad peaks located $\approx q$ = 1.5, 3, and 5.2 $Å^{-1}$ in the pattern of pristine sample correspond to the 002, 100, and 110 diffractions of graphite-like structure in HC. Along with peaks corresponding to the host carbon structure, additional scattering peaks were observed for the sodiated HC, which can be attributed to metallic Na crystals. These SAXS and WAXS results are consistent with the WAXS data reported by Morikawa et al.[23] and the X-ray total scattering observed by Stratford et al.,[24] confirming that the large capacity of HC-Zn is indeed due to the formation of sodium clusters within the nanopores. The completely reversible change in the WAXS and SAXS patterns during sodium insertion and extraction proves that the electrochemical formation and removal of Na clusters within these nanopores is a highly reversible process. Because HC-Zn showed superior performance in the Na cells, we further optimized HC-Zn by diluting and enriching the amount of ZnO in the carbon matrix.

2.4. Dilution and Enrichment of ZnO as Nanopore Template

The size and distribution of the ZnO templates are expected to be critical factors for enhancing Na storage capacity. Thus, we investigated the effect of template dilution and enrichment on the capacity of the ZnO-template HCs by introducing glucose (Glc) as an additional carbon source and zinc acetate ($Zn(OAc)_2$) as an additional template source for Zn Glu. According to the literature, only ZnO remains after the pyrolysis of $Zn(OAc)_2$ even in an inert gas atmosphere,[47] and the C-atoms in acetate ions are removed as CO_2 or acetone.[48] Therefore, the amount of ZnO in the preheated precursors derived from the mixtures of Zn Glu and $Zn(OAc)_2$ was reasonably expected to be greater than that in PRE-Zn.

The starting materials were prepared by homogeneously mixing Glc, Zn, Glu, and $Zn(OAc)_2$ via freeze-drying (see Supporting Information for details). The samples are designated as PRE-Zn[*x*-*y*-*z*], wPRE- Zn[*x*-*y*-*z*], or HC-Zn[*x*-*y*-*z*] where the mixing molar ratio of Glc, Zn Glu, and $Zn(OAc)_2$ is expressed as $x:y:z$, which is appended after "Zn. " The freeze-drying process was employed for pure Zn Glu for comparison; thus, the sample preparation conditions of HC-Zn[0-100-0] differed slightly from those of HC-Zn, even though both originated from pure Zn Glu.

The XRD patterns of the unwashed and washed precursors, as well as the HCs, are shown in Figure S10 (Supporting Information). The synthesis process of the HCs appeared to be consistent as there were no significant differences in the patterns, except for variations in the intensity and breadth of the ZnO diffraction peaks. The crystallite sizes of ZnO in PRE-Zn[*x*-*y*-*z*] and wPRE-Zn[*x*-*y*-*z*], calculated in the same manner as shown in Figure S5 (Supporting Information), are summarized in Table S1 (Supporting Information). The crystallite sizes of ZnO calculated from Scherrer's equation with broad diffraction peaks derived from ZnO nanoparticles, which are available as templates for nanopores, showed no substantial variation with different mixing ratios of raw materials. Even with an increasing amount of template, the Zn residue was hardly detected in the final product, HC, because ZnO was reduced, and the resultant Zn metal was volatilized during the post-heat treatment, as evidenced by the STEM-EDS mapping of HC[0-75-25] in Figure S11 (Supporting

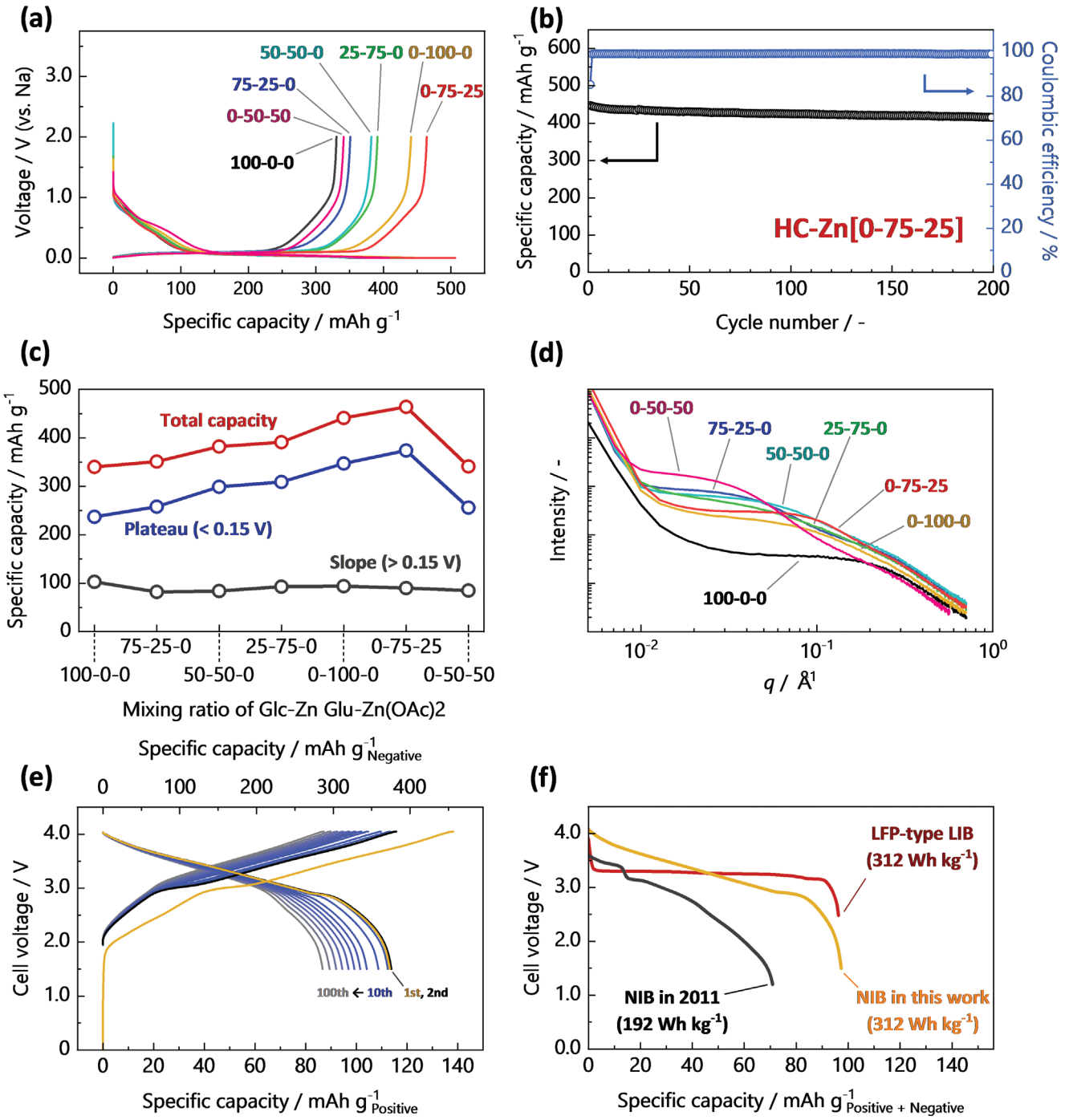

Figure 4. a) Initial charge–discharge curves of HC-Zn[*x*-*y*-*z*] in Na half-cell. b) Cycle performance of HC-Zn[0-75-25] in Na half-cell. c) Relationship between mixing ratio of the raw materials and the specific capacity of corresponding HCs. d) SAXS patterns of HC-Zn[*x*-*y*-*z*]. e) Charge–discharge curves of $Na_{5/6}Ni_{1/3}Fe_{1/6}Mn_{1/6}Ti_{1/3}O_2$//HC-Zn[0-75-25] full cell. f) Comparison of gravimetric energy densities among NIB in this study, NIB reported in 2011 in ref. [3] and LIB consisting of $LiFePO_4$ and graphite.

Information). Although a sample derived from a mixture of Glc, Zn Glu, and $Zn(OAc)_2$ in the ratio of 100:0:0 contains no Zn at all, the sample is formally denoted as "HC-Zn[100-0-0]" for simplicity. The XRD patterns of PRE-Zn[100-0-0] and HC-Zn[100-0-0], shown in Figure S12 (Supporting Information), confirm the absence of crystalline ZnO in the sample.

Figure 4a shows the initial charge and discharge curves of HCs synthesized from a freeze-dried mixture with different ratios of Glc, Zn Glu, and $Zn(OAc)_2$. In Figure 4a, the dilution of the template by the addition of Glc to Zn Glu resulted in a decrease in the capacity. On the contrary, enrichment of the template by adding 25% $Zn(OAc)_2$ effectively enhanced a reversible capacity up to

464 mAh g^{-1} (corresponding to $NaC_{4.8}$ formation by assuming no irreversible Na insertion) and high initial Coulombic efficiency of 91.7% for HC-Zn[0-75-25]. Although the sodiation potential of HC-Zn[0-75-25] is close to the Na plating potential, it was comparable to that of HC-Zn and the previously reported MgO template HC, as shown in Figure S13 (Supporting Information).

Figure 4b reveals that HC-Zn[0-75-25] electrode exhibits good long-term cycling stability over 200 cycles, and its capacity retention after 200 cycles was 93% of the initial capacity. The cycle performance was not compromised, even with a 48 mAh g^{-1} increase in capacity compared to that of HC-Zn (418 mAh g^{-1}), as shown in Figure 3. Although several HCs with enhanced capacities of ≈500 mAh g^{-1} have been reported in recent years,[13,14,16,17,49] there are no other reports of HCs that possess all of sufficient cycle stability, high initial efficiency (>90%), and minimal potential hysteresis leading to high energy efficiency, aside from MgO-template HCs.[15] Since a high initial Coulombic efficiency is an essential requirement for practical full-cell operation,[50] the template synthesis method is believed to be very effective in increasing the energy density of NIB full cells.

In Figure 4c, the total initial capacity, capacity of the plateau region (<0.15 V), and that of the slope region (>0.15 V) of the ZnO-template HCs are plotted against the composition of the raw materials. The slope capacity of the HCs was nearly constant and independent of the composition of the raw materials, and the variation in the total capacity was primarily dominated by that of the plateau region. In general, the plateau capacities of HCs strongly depend on their closed-pore structure. Therefore, a high reversible capacity could be achieved by varying the amount and distribution of the ZnO template. Actually, we found that HC-Zn[0-75-25], with the minor addition of $Zn(OAc)_2$ to Zn Glu, demonstrated the maximum capacity, whereas HC-Zn[0-50-50], with an increased $Zn(OAc)_2$ quantity of 50%, presented only 341 mAh g^{-1} as seen in Figure 4c. This result indicates that there is an optimum amount of ZnO as a template for nanopores. Our previous work showed that a MgO-template HC derived from a 50:50 mixture of Mg Glu, and Glc exhibited a maximum capacity of 478 mAh g^{-1}. The difference in optimum values for the MgO and ZnO template amounts can be attributed to differences in the crystallite size, crystallinity, and grain size distribution of MgO and ZnO embedded in the carbon precursors, as discussed above.

The relationship between the mixing ratio of the raw materials and the Na storage performance can be elucidated from the structural characteristics of the HCs. The pore structures of the HCs were characterized using SAXS, as shown in Figure 4d. The shoulder peak profiles varied significantly depending on the mixing ratio of the raw materials. In particular, HC-Zn[0-50-50] possessed an unusual pattern with a notably larger peak than the other samples in the region q = 0.02–0.03 $Å^{-1}$. According to the XRD results in Figure S10 (Supporting Information), the broad diffraction peaks of ZnO were barely noticeable in the patterns of PRE-Zn [0-50-50] and wPRE-Zn[0-50-50], suggesting that the formation of fine ZnO template nanoparticles was limited in these samples. Excessive addition of $Zn(OAc)_2$ likely led to the overgrowth of ZnO crystals, thereby reducing the fraction of fine ZnO nanoparticles suitable as templates for nanopores.

The HCs derived from the mixtures containing Glc also exhibited SAXS patterns that could not be satisfactorily fitted to a single peak. Our analysis requires the assumption of two shoulder peaks to fit the patterns of HC-Zn[75-25-0], HC-Zn, [50-50-0], and HC-Zn[25-75-0] (see Figure S14a—c, Supporting Information). However, for Glc-free HC-Zn[0-100-0] and HC-Zn[0-75-25], a single peak was observed to fit the experimental data (Figure S14d,e, Supporting Information). The structural parameters of HC-Zn[x-y-z], such as the interlayer distance d_{002}, crystallite size of the pseudo-graphitic domain L_c, stacking number calculated from the XRD data, and pore size D_{SAXS} are summarized in Table S2 (Supporting Information). According to our experience and recent studies on HC, it is still challenging to determine a straightforward relationship between these parameters and Na storage capacity because of the difficulty in distinguishing between extended interlayers in the pseudo-graphitic domains and nanopores along with a highly disordered framework, and thus these parameters roughly correlate with each other.[24] However, as a general trend, the large-capacity HCs in this study have the following features: 1) they possess a large d_{002} and small L_c, and therefore a small number of stacking layers n; 2) their size distribution, as observed by SAXS, is highly uniform, and the average pore size is relatively large. This trend was also supported by the focused ion beam processed (FIB)-STEM observations of HC-Zn[25-75-0] and HC-Zn[0-75-25], as shown in Figure S15 (Supporting Information). The high-magnification STEM image of HC-Zn[25-75-0] confirms a heterogeneous structure with a void-like structure of ≈5 nm, whereas the HC-Zn[0-75-25] sample has a dense structure with high uniformity. The 5 nm scale pore-like structure observed in the STEM image of HC-Zn[25-75-0] is consistent with the pore diameter of 4.34 nm calculated from the low-q peak in the SAXS pattern of HC-Zn[25-75-0] (see Table S2, Supporting Information). Therefore, we conclude that optimizing the mixing ratio of the raw materials and achieving a uniform distribution of nanopores with a suitable size for Na clustering maximizes the capacity of the ZnO-template carbons. This consideration is in agreement with the recent discussion by Stratford et al., describing the pore size distribution is more important than the average pore size in controlling the Na storage capacity.[24]

A Na-ion full cell consisting of HC-Zn[0-75-25], which exhibits a superior reversible capacity as a negative electrode material, and a Na-containing layered transition oxide $Na_{5/6}Ni_{1/3}Fe_{1/6}Mn_{1/6}Ti_{1/3}O_2$ as a positive electrode material[51] were fabricated with 1 mol dm^{-3} $Na(PF_6)_{0.8}(FSA)_{0.2}$/EC:PC (1:1 v/v) solution with the addition of 0.2 vol% vinylene carbonate. Although the reversible capacity of HC-Zn[0-75-25] is slightly smaller than that of HC-Mg, [50-50-0] the optimized MgO-template HC in ref., [15] the simulated discharge curves of the full cells are almost identical as shown in Figure S16 (Supporting Information), partly because the former exhibits a better initial coulombic efficiency that the latter. The charge–discharge curves of the NIB are shown in Figure 4e, and their capacity retention over 100 cycles is shown in Figure S17a (Supporting Information). The specific capacity of 113 mAh g^{-1} based on positive electrode mass (corresponding to 373 mAh g^{-1} based on negative electrode mass) was demonstrated at the initial cycle, and satisfactory cycle performance was achieved over the subsequent 100 cycles. The discharge rate capability of the NIB full cell is shown in Figure S17b (Supporting Information). The capacity and cell polarization are hardly changed and deteriorated by increasing

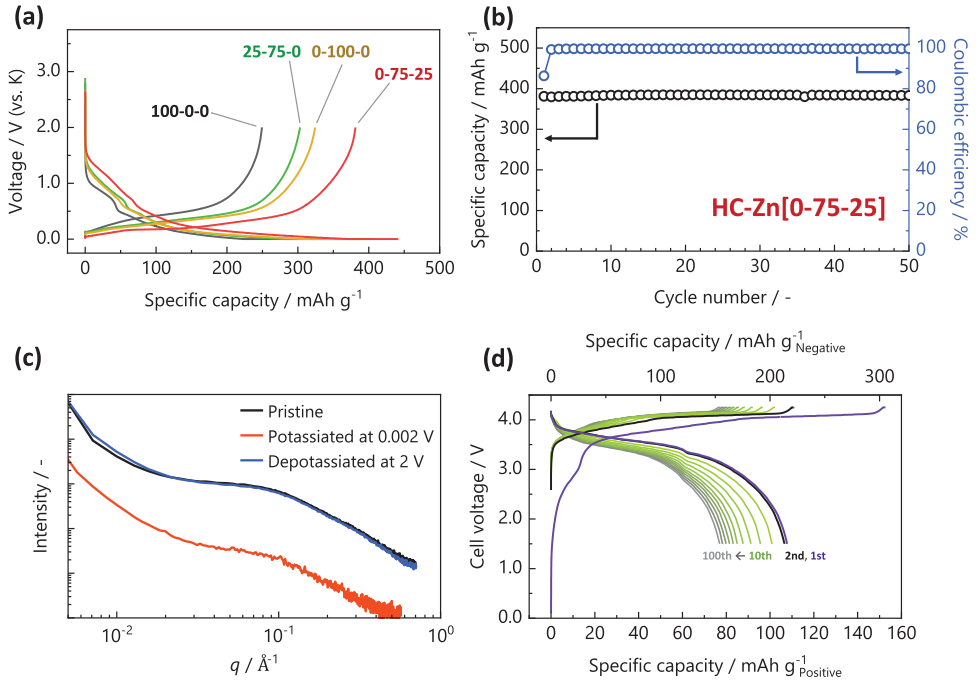

Figure 5. a) Initial charge–discharge curves of HC-Zn[*x*-*y*-*z*] in K half-cell. b) Cycle performance of HC-Zn[0-75-25] in K half-cell. c) ex situ SAXS patterns of HC-Zn in different potassiation states. d) Charge–discharge curves of $K_2Mn[Fe(CN)_6]$//HC-Zn[0-75-25] full cell.

current rates from 0.1 to 1 C. Even at a high rate of 10 C, the cell retained ≈76% of its capacity compared to that at 0.1 C, demonstrating the robust rate capability of the full cell.

The discharge curves and gravimetric energy densities of the NIB cells fabricated in this study, those from a 2011 study,[3] and those of a conventional LIB consisting of $LiFePO_4$ (LFP) and graphite were experimentally compared under comparable test conditions, as shown in Figure 4f. The energy density of NIB fabricated in this study reached 312 Wh kg^{-1}. This value is >1.5 times larger than that of the O3-type layered $NaNi_{0.5}Mn_{0.5}O_2$//Kureha's HC Na-ion cell reported in 2011, which was one of the earliest demonstrations of NIBs free from Na-metal electrodes, and it is comparable to the energy density of widely commercialized LFP-type LIB. Although there remain challenges, such as the longer cycle life of a full cell and Ni-free high-capacity positive electrode, we succeeded in developing a large-capacity and high-initial coulombic efficiency HC-Zn[0-75-25] material, which enables NIB to have a comparable or higher energy density than LIBs.

2.5. Application to KIB Negative Electrodes

The ZnO-template HCs were further applied as negative electrodes in KIBs. The charge and discharge curves (corresponding to potassium insertion and extraction, respectively) of the K half-cells are shown in **Figure 5**a. Because the potential variation and reversibility were similar to those of potassium insertion into HC reported previously,[6,39,40] the redox activity was caused by reversible electrochemical potassium insertion. For these ZnO-template HCs, the specific capacity of the K cells followed a trend consistent with that of the Na cells. For instance, HC-Zn[0-75-25], which exhibits the largest capacity in a Na half-cell, also demonstrated a large capacity of 381 mAh g^{-1} in a K half-cell. This reversible capacity corresponds to $KC_{5.8}$ formation by assuming all charges passing through the electrode are consumed for K insertion. The K concentration was higher than that of stage-1 KC_8 and the Li concentration of stage-1 LiC_6. The trend of high Na storage capacity in HCs correlating with high K storage capacity is commonly observed in conventional HCs derived from cellulose,[39] sucrose,[6] and phenolic resins.[40] The high reversibility of HC-Zn[0-75-25] over 50 cycles (Figure 5b) can be attributed to the reversible K insertion into the carbon structure rather than the plating/stripping of K metal.

Given that several samples delivered large reversible capacities, far exceeding the theoretical capacity of graphite in K cells (279 mAh g^{-1} for KC_8 chemical composition),[52] it is reasonable to conclude that K storage sites can accommodate K atoms at significantly higher concentrations than the KC_8 in-plane arrangement typically found in K-GICs. A recent study suggested the possibility of the formation of quasi-metallic K clusters in the closed pores of HC materials.[53,54] It has been suggested that the size of the closed pores suitable for alkali metal clustering depends on the alkali metal species, and Na clustering requires a larger pore size than that of Li.[26] In fact, the HCs developed in this study had smaller capacities in the Li half-cells than in the Na and K half-cells, as shown in Figure S18 (Supporting Information). To understand the mechanism of K-insertion, ex situ SAXS measurements were performed. Figure 5c displays the ex situ SAXS patterns of pristine, potassiated, and depotassiated HC-Zn (see the initial charge–discharge curves in Figure S19, Supporting Information). The identical SAXS patterns of the pristine and depotassiated samples indicate that K insertion is completely reversible. Contrastingly, the pattern of the potassiated sample shows a

decrease in the scattering intensity over a wide q range. Similar to the pattern of the sodiated sample (Figure 3c), the decrease in the shoulder peak intensity indicates a reduction in the electron density contrast between the nanopores and carbon matrix. Therefore, we anticipate the formation of K clusters in HC in the low-potential region based on the correlation between the Na and K-storage capacities in various HCs[6,39,40] as well as the notable K-storage capacity of the ZnO-template HC, which clearly exceeds the stoichiometric KC_8 composition. A comparison of the energy densities of hypothetical KIB full cells with graphite or HC-Zn[0-75-25] as negative electrodes is shown in Figure S20 (Supporting Information). Because the average depotassiation potentials of graphite and HC-Zn[0-75-25] are 0.37 and 0.41 V versus K^+/K, respectively, HC-Zn[0-75-25] has a disadvantageous working potential. However, the energy density of the hypothetical full cell per weight of the negative electrode is much higher for HC-Zn[0-75-25] than for graphite owing to its anomalously large capacity.

Given that ZnO-template HCs were found to deliver a larger capacity as negative electrodes for KIBs, a KIB full cell consisting of $K_2Mn[Fe(CN)_6]$ and HC-Zn[0-75-25] with a 1 mol dm^{-3} $K(PF_6)_{0.8}(FSA)_{0.2}$/EC:PC solution[55] + 0.2 vol% vinylene carbonate was fabricated with an optimal mass ratio of 2.0:1 for the positive and negative electrodes. The charge–discharge curves and cycle performance are shown in Figure 5d and Figure S21 (Supporting Information), respectively. The KIB showed an average discharge voltage of 3.3 V and a substantial specific capacity of 107 mAh (g of $K_2Mn[Fe(CN)_6])^{-1}$, without any pretreatment of the electrolyte and electrodes, such as pre-cycling. These results confirm that a large-capacity HC is compatible with KIBs when combined with proper positive electrodes and is a promising alternative to graphite for KIB-negative electrodes.[56] We believe that a new series of templated porous carbon materials has potential as active materials for next-generation batteries, such as NIB and KIB, and will possibly be enhanced by rational design depending on the battery and redox system for future energy devices.

3. Conclusion

A novel ZnO-template HC featuring large capacity, high initial Coulombic efficiency, and low working potential for negative electrodes suitable for Na- and KIBs was developed. Systematic characterization and electrochemical evaluation of the precursors and HCs derived from Mg Glu, Zn Glu, and Ca Glu suggested that the ZnO-template carbon is a promising NIB negative electrode, comparable to the MgO-template HC. A ZnO-template HC derived from a mixture of Zn Glu and $Zn(OAc)_2$ in an appropriate mixing ratio exhibited a maximum capacity of 464 mAh g^{-1}. Based on comprehensive experiments on the structure and electrochemical properties of various samples derived from Glc–Zn Glu–$Zn(OAc)_2$ mixtures with different mixing ratios, the large capacity of the optimized ZnO-template HC was attributed to its favorable pore size and uniform pore distribution for Na clustering. An NIB full cell with a ZnO-template HC provides an energy density of over 300 Wh kg^{-1}, which is comparable to that of LFP-based LIBs, overcoming the challenges associated with the heavy atomic weight of Na and the high standard electrode potential of Na^+/Na. Furthermore, an unprecedented large K-storage capacity was also found for the ZnO-template HCs, and a KIB full cell with a ZnO-template HC without any precycling treatment was successfully demonstrated. This finding proves that HCs are promising candidates for KIB negative electrodes as an alternative to graphite. We hope that this study will trigger improvements in the energy densities of NIBs and KIBs to a new level beyond that of LIBs.

Supporting Information

Supporting Information is available from the Wiley Online Library or from the author.

Acknowledgements

This study was partially funded by the MEXT Program, Data Creation, and Utilization Type Materials Research and Development Project (grant no. JPMXP 1122712807) and JST-CREST (grant no. JPMJCR21O6), the NEDO Intensive Support Program for Young Promising Researchers (grant no. JPNP20004), and JSPS KAKENHI (Grant No. JP20H02849, JP21K14724, JP21K20561, JP22K14772, and JP23K13829). The authors are grateful to Dr. Toshinari Ichihashi and Prof. Yasushi Idemoto at the Tokyo University of Science for the TEM measurements and to Haruka Yoshimo, Kazushi Magara, Nobuhito Noro, Tatsuo Matsuyama, Yuki Fujii, and Yuki Hoshi for their experimental support. D.I. thanks the JST for establishing university fellowships for the Creation of Science and Technology Innovation (grant no. JPMJFS2144), and the academic crowdfunding platform "academist" and its supporters. R.T. thanks the TEPCO Memorial Foundation research grant (basic research), the ECSJ Kanto branch research grant, and the Takahashi Industrial and Economic Research Foundation.

Conflict of Interest

The authors declare no conflict of interest.

Data Availability Statement

The datasets in this study are available from the corresponding author on reasonable request.

Keywords

anode materials, hard carbon, K-ion batteries, Na-ion batteries, nanopores, template synthesis

Received: August 12, 2023
Revised: September 11, 2023
Published online: November 9, 2023

[1] N. Yabuuchi, K. Kubota, M. Dahbi, S. Komaba, *Chem. Rev.* **2014**, *114*, 11636.
[2] T. Hosaka, K. Kubota, A. S. Hameed, S. Komaba, *Chem. Rev.* **2020**, *120*, 6358.
[3] S. Komaba, W. Murata, T. Ishikawa, N. Yabuuchi, T. Ozeki, T. Nakayama, A. Ogata, K. Gotoh, K. Fujiwara, *Adv. Funct. Mater.* **2011**, *21*, 3859.
[4] Y. Kondo, T. Fukutsuka, K. Miyazaki, Y. Miyahara, T. Abe, *J. Electrochem. Soc.* **2019**, *166*, A5323.

[5] H. Au, H. Alptekin, A. C. S. Jensen, E. Olsson, C. A. O'keefe, T. Smith, M. Crespo-Ribadeneyra, T. F. Headen, C. P. Grey, Q. Cai, A. J. Drew, M.-M. Titirici, *Energy Environ. Sci.* **2020**, *13*, 3469.
[6] K. Kubota, S. Shimadzu, N. Yabuuchi, S. Tominaka, S. Shiraishi, M. Abreu-Sepulveda, A. Manivannan, K. Gotoh, M. Fukunishi, M. Dahbi, S. Komaba, *Chem. Mater.* **2020**, *32*, 2961.
[7] H. Alptekin, H. Au, A. C. Jensen, E. Olsson, M. Goktas, T. F. Headen, P. Adelhelm, Q. Cai, A. J. Drew, M.-M. Titirici, *ACS Appl. Energy Mater.* **2020**, *3*, 9918.
[8] K. Tatsumi, J. Conard, M. Nakahara, S. Menu, P. Lauginie, Y. Sawada, Z. Ogumi, *J. Power Sources* **1999**, *81–82*, 397.
[9] Z. Jian, Z. Xing, C. Bommier, Z. Li, X. Ji, *Adv. Energy Mater.* **2016**, *6*, 1501874.
[10] J. R. Dahn, *Phys. Rev. B* **1991**, *44*, 9170.
[11] H. Onuma, K. Kubota, S. Muratsubaki, W. Ota, M. Shishkin, H. Sato, K. Yamashita, S. Yasuno, S. Komaba, *J. Mater. Chem. A* **2021**, *9*, 11187.
[12] Y. Nishi, *Chem. Rec.* **2001**, *1*, 406.
[13] J. Chen, T. Hu, Z. Zou, Q. Zeng, Y. Jiang, C. Tang, C. Tang, W. Li, C. Fang, W. Sun, L. Zeng, C. M. Li, *Carbon* **2022**, *186*, 193.
[14] Z. Lu, J. Wang, W. Feng, X. Yin, X. Feng, S. Zhao, C. Li, R. Wang, Q.-A. Huang, Y. Zhao, *Adv. Mater.* **2023**, *35*, 2211461.
[15] A. Kamiyama, K. Kubota, D. Igarashi, Y. Youn, Y. Tateyama, H. Ando, K. Gotoh, S. Komaba, *Angew. Chem., Int. Ed.* **2021**, *60*, 5114.
[16] Q. Li, X. Liu, Y. Tao, J. Huang, J. Zhang, C. Yang, Y. Zhang, S. Zhang, Y. Jia, Q. Lin, Y. Xiang, J. Cheng, W. Lv, F. Kang, Y. Yang, Q.-H. Yang, *Natl. Sci. Rev.* **2022**, *9*, nwac084.
[17] X. Yin, Z. Lu, J. Wang, X. Feng, S. Roy, X. Liu, Y. Yang, Y. Zhao, J. Zhang, *Adv. Mater.* **2022**, *34*, 2109282.
[18] V. L. Deringer, C. Merlet, Y. Hu, T. H. Lee, J. A. Kattirtzi, O. Pecher, G. Csányi, S. R. Elliott, C. P. Grey, *Chem. Commun.* **2018**, *54*, 5988.
[19] Y. Youn, B. Gao, A. Kamiyama, K. Kubota, S. Komaba, Y. Tateyama, *NPJ Comput. Mater.* **2021**, *7*, 48.
[20] J. Li, C. Peng, J. Li, J. Wang, H. Zhang, *Energy Fuels* **2022**, *36*, 5937.
[21] D. A. Stevens, J. R. Dahn, *J. Electrochem. Soc.* **2000**, *147*, 4428.
[22] D. A. Stevens, J. R. Dahn, *J. Electrochem. Soc.* **2001**, *148*, A803.
[23] Y. Morikawa, S.-I. Nishimura, R.-I. Hashimoto, M. Ohnuma, A. Yamada, *Adv. Energy Mater.* **2020**, *10*, 1903176.
[24] J. M. Stratford, A. K. Kleppe, D. S. Keeble, P. A. Chater, S. S. Meysami, C. J. Wright, J. Barker, M.-M. Titirici, P. K. Allan, C. P. Grey, *J. Am. Chem. Soc.* **2021**, *143*, 14274.
[25] J. M. Stratford, P. K. Allan, O. Pecher, P. A. Chater, C. P. Grey, *Chem. Commun.* **2016**, *52*, 12430.
[26] R. Morita, K. Gotoh, M. Fukunishi, K. Kubota, S. Komaba, N. Nishimura, T. Yumura, K. Deguchi, S. Ohki, T. Shimizu, H. Ishida, *J. Mater. Chem. A* **2016**, *4*, 13183.
[27] J. S. Weaving, A. Lim, J. Millichamp, T. P. Neville, D. Ledwoch, E. Kendrick, P. F. Mcmillan, P. R. Shearing, C. A. Howard, D. J. L. Brett, *ACS Appl. Energy Mater.* **2020**, *3*, 7474.
[28] T. Morishita, T. Tsumura, M. Toyoda, J. Przepiórski, A. W. Morawski, H. Konno, M. Inagaki, *Carbon* **2010**, *48*, 2690.
[29] T. Kyotani, Z. Ma, A. Tomita, *Carbon* **2003**, *41*, 1451.
[30] A. A. Zakhidov, R. H. Baughman, Z. Iqbal, C. Cui, I. Khayrullin, S. O. Dantas, J. Marti, V. G. Ralchenko, *Science* **1998**, *282*, 897.
[31] B. Yan, J. Zheng, F. Wang, L. Zhao, Q. Zhang, W. Xu, S. He, *Mater. Des.* **2021**, *201*, 109518.
[32] C. Zhao, W. Wang, Z. Yu, H. Zhang, A. Wang, Y. Yang, *J. Mater. Chem.* **2010**, *20*, 976.
[33] Y. Maeno, K. Hagino, T. Ishiguro, *Found. Chem.* **2021**, *23*, 201.
[34] E. R. Buiel, A. E. George, J. R. Dahn, *Carbon* **1999**, *37*, 1399.
[35] B.-S. Kim, J.-M. Yoo, J.-T. Park, J.-C. Lee, *Mater. Trans.* **2006**, *47*, 2421.
[36] P. Strubel, S. Thieme, T. Biemelt, A. Helmer, M. Oschatz, J. Brückner, H. Althues, S. Kaskel, *Adv. Funct. Mater.* **2015**, *25*, 287.
[37] F. J. W. J. Labuschagné, W. W. Focke, *J. Mater. Sci.* **2003**, *38*, 1249.
[38] K. Omote, Y. Ito, S. Kawamura, *Appl. Phys. Lett.* **2003**, *82*, 544.
[39] H. Yamamoto, S. Muratsubaki, K. Kubota, M. Fukunishi, H. Watanabe, J. Kim, S. Komaba, *J. Mater. Chem. A* **2018**, *6*, 16844.
[40] A. Kamiyama, K. Kubota, T. Nakano, S. Fujimura, S. Shiraishi, H. Tsukada, S. Komaba, *ACS Appl. Energy Mater.* **2020**, *3*, 135.
[41] M. Thommes, K. Kaneko, A. V. Neimark, J. P. Olivier, F. Rodriguez-Reinoso, J. Rouquerol, K. S. W. Sing, *Pure Appl. Chem.* **2015**, *87*, 1051.
[42] J. Tan, Z. Li, M. Ye, J. Shen, *ACS Appl. Mater. Interfaces* **2022**, 37259.
[43] G. Duan, J. Xiao, L. Chen, C. Zhang, S. Jian, S. He, F. Wang, *J. Energy Storage* **2023**, *67*, 107559.
[44] L.-J. He, J.-Q. Zhong, Y.-M. Liu, Z.-J. Zhou, W.-H. Yang, *ChemistrySelect* **2020**, *5*, 12759.
[45] Z. V. Bobyleva, O. A. Drozhzhin, A. M. Alekseeva, K. A. Dosaev, G. S. Peters, G. P. Lakienko, T. I. Perfilyeva, N. A. Sobolev, K. I. Maslakov, S. V. Savilov, A. M. Abakumov, E. V. Antipov, *ACS Appl. Energy Mater.* **2023**, *6*, 181.
[46] H. Yang, J. Hwang, Y. Tonouchi, K. Matsumoto, R. Hagiwara, *J. Mater. Chem. A* **2021**, *9*, 3637.
[47] N. Horzum, M. E. Hilal, T. Isik, *New J. Chem.* **2018**, *42*, 11831.
[48] A. Moezzi, A. Mcdonagh, A. Dowd, M. Cortie, *Inorg. Chem.* **2013**, *52*, 95.
[49] S. Li, H. Yuan, C. Ye, Y. Wang, L. Wang, K. Ni, Y. Zhu, *J. Mater. Chem. A* **2023**, *11*, 9816.
[50] J. A. S. Oh, G. Deysher, P. Ridley, Y.-T. Chen, D. Cheng, A. Cronk, S.-Y. Ham, D. H. S. Tan, J. Jang, L. H. B. Nguyen, Y. S. Meng, *Adv. Energy Mater.* **2023**, *13*, 2300776.
[51] S. Komaba, *Chem. Lett.* **2020**, *49*, 1507.
[52] Z. Jian, W. Luo, X. Ji, *J. Am. Chem. Soc.* **2015**, *137*, 11566.
[53] Q. Li, J. Zhang, L. Zhong, F. Geng, Y. Tao, C. Geng, S. Li, B. Hu, Q.-H. Yang, *Adv. Energy Mater.* **2022**, *12*, 2201734.
[54] A. Vasileiadis, Y. Li, Y. Lu, Y.-S. Hu, M. Wagemaker, *ACS Appl. Energy Mater.* **2023**, *6*, 127.
[55] T. Hosaka, T. Matsuyama, K. Kubota, S. Yasuno, S. Komaba, *ACS Appl. Mater. Interfaces* **2020**, *12*, 34873.
[56] X. Bie, K. Kubota, T. Hosaka, K. Chihara, S. Komaba, *J. Mater. Chem. A* **2017**, *5*, 4325.